Geometrically coherent continuous deformation in the volume surrounding a seismically imaged normal fault-array

J.J. Long[1]* and J. Imber[1]

[1]Department of Earth Sciences, Durham University, Durham, UK

* Corresponding author.

E-mail address: jonathan.long@durham.ac.uk

Fax: +44 0191 3342301

Keywords

Fault-propagation folds; Normal fault; Geometric coherence; Seismic resolution; Sub-seismic faults

Abstract

We calculated an apparent dip attribute, which was used to ascertain the spatial distribution of fault-related continuous deformation. The vertical component of displacement calculated from the continuous deformation acts to “fill-in” missing displacement in the fault-throw profile. This result shows that apparently complex 3D patterns of continuous strain in the volumes surrounding the fault-array developed as part of a single, geometrically coherent fault-array. However, if this component of continuous deformation was not added to the throw profile, the fault-array could have been misinterpreted as a series of isolated fault segments with coincidental overlaps. This technique permits the analysis of continuous deformation structures, which are up to an order of magnitude smaller than previously described. In the study area, these structures are interpreted as small

fault-propagation folds, forming in a shale-dominated cover sequence. The fault-propagation folds above the upper tip line of the mapped fault-array bifurcate upwards from the fault surface into three coherent lobes and resemble secondary fault segments. The near-constant along-strike length of the region of continuous deformation throughout the syn-rift sequence implies that the length of the fault-array was established at an early stage in its growth, prior to the establishment of a seismically-visible fault surface.

1. Introduction

Fault-arrays comprise multiple fault segments (Peacock and Sanderson, 1991; Childs et al., 1995; Childs et al., 1996a; Willemse, 1997; Crider and Pollard, 1998; Peacock, 2002) that typically grow as geometrically coherent structures (Walsh and Watterson, 1991; Childs et al., 1995; Walsh et al., 2003b). Fault segments within these arrays can be hard-linked by discrete faults or soft-linked by zones of continuous deformation (Peacock and Sanderson, 1991; Trudgill and Cartwright, 1994; Childs et al., 1995; Walsh et al., 2003b). In seismic reflection profiles, continuous deformation is commonly expressed as the rotation, thickening or thinning of strata within the deformed volume between soft-linked faults. Continuous strains result from any combination of plastic deformation and/or small-scale faults or fractures below the resolvable limits of seismic data (e.g. Fig. 1; (Steen et al., 1998; Townsend et al., 1998). The specific limits at which structures can be resolved depend on the depth of the feature and the quality of the seismic data.

Geometric coherence is the concept that faults and fault-related strain maintain regular and systematic geometries and relationships throughout the evolution of a fault-array. The throws due to faults and associated continuous deformation should together produce smoothly varying displacement profiles, which resemble that of a single fault (Walsh et al., 2003b). If a fault-array has maintained geometric coherence this must suggest kinematic coherence, which is the systematic and linked accumulation of displacement across the fault-array (Walsh and Watterson, 1991). The fault-propagation model of Marchal et al. (1998) predicts that fault-arrays evolve by the coherent growth and linkage of secondary faults, which are small faults that form at the propagating tips of a primary fault

segment. Secondary faults can form as separate fault segments soft-linked to the primary fault via relay zones, or as hard-linked structures that bifurcate from the main fault surface. This fault growth model can be applied to both horizontal and vertical tip lines (Marchal et al., 1998; Marchal et al., 2003). Fault-propagation will ultimately result in segmented fault tip lines, as shown by observations of naturally occurring faults (Mcgrath and Davison, 1995; Childs et al., 1996b; Marchal et al., 2003; Kristensen et al., 2008)

Fault-propagation folds are manifestations of fault-related continuous deformation that develop ahead of a propagating tip line and which deform the free surface (Withjack et al., 1990; Corfield and Sharp, 2000; Sharp et al., 2000; Gawthorpe et al., 2003; Finch et al., 2004; Jackson et al., 2006; White and Crider, 2006; Ford et al., 2007). In the case of synsedimentary normal faults, fault-propagation folds are expressed as monoclines whose axes lie parallel to the strike of the fault-array. The development of a synsedimentary monocline results in the main depocentre being offset into the hanging wall, in comparison with emergent synsedimentary normal faults where the depocentre is located in the immediate hanging wall of the fault (Sharp et al., 2000; Gawthorpe et al., 2003). Scaled analogue and numerical models of extensional fault-propagation folds above rigid basement fault blocks have shown that the amplitudes and wavelengths of monoclines are controlled by the dip of the basement fault and by the rheology of the overlying strata. These models also show that the mechanical stratigraphy controls whether fault-arrays within the cover are isolated or hard-linked to the basement fault (Withjack and Callaway, 2000; Finch et al., 2004).

The aim of this paper is to describe the three dimensional (3D) geometry of the brittle and continuous deformation at and beyond the upper tips of a

synsedimentary normal fault-array in the Inner Moray Firth basin (IMF). However, the method and applications are not limited to synsedimentary settings, or to the IMF. We use interpretations of 3D seismic reflection data to test the idea that deformation at seismically imaged fault tips, including continuous deformation, is geometrically coherent. The methodology described here allows us to make inferences about the complex geometric arrangement of secondary faults, on which the offsets are below the resolution of the seismic data and are therefore manifest, at least in part, as continuous deformation at the scale of observation. The scale of structures studied in this paper (maximum throw ca. 115 ms) is greater than those described by (Kristensen et al., 2008), but less than those of (Corfield and Sharp, 2000).

2. Geological setting

The study area is located in the Inner Moray Firth basin (Fig. 2). The main phase of NW-SE extension occurred during the Late Jurassic to Early Cretaceous (represented by the mapped H5 to BCU interval; Figs 3 and 4). There is little evidence for active extension during the Triassic to Mid-Oxfordian, which is represented by the mapped Triassic chert to Horizon H5 interval (Figs 3 and 4). This extension produced the regional NE-SW trending normal fault set (Fig. 2c) (Underhill, 1991b; Thomson and Underhill, 1993) and associated half-graben basin fill (Fig. 2) (Underhill, 1991b). Sediment packages thicken towards the north-west along the Helmsdale–Wick boundary fault systems (Fig. 2). Subsequent Cretaceous sedimentation records gentle regional subsidence. Post-Cretaceous reactivation of some large-offset faults has occurred in the IMF. Faults that offset the BCU are recognised as being reactivated, but no evidence is

found for post-Cretaceous deformation having reactivated faults in the immediate study area.

The study focuses on deformation within the Middle to Upper Jurassic succession, which encompasses the uppermost part of the pre-rift and lowermost syn-rift sequences (Figs 3 and 4). Regionally, the onset of syn-rift sedimentation was marked by deposition of the H5 horizon (Intra Oxfordian reflector). Correlation of seismic reflectors with nearby wells shows that the mapped syn-rift sequence (H5-H1) is shale-dominated and overlies a sandstone-dominated pre-rift sequence, which includes Horizon H6 (Fig. 4).

The mapped fault-array consists of three NE-SW trending en-echelon segments (F1-F3; Fig. 3) separated by two relay zones. Aggregate displacement on the array decreases southwest towards the mapped lateral tips. The studied faults dip towards the NW, antithetic to nearby large offset faults that dip towards the SE (Fig. 3).

The mapped H1-H5 sequence thickens from footwall to hanging wall across F1, F2 and F3 (Fig. 3). Fault scraps in the IMF show no evidence for footwall erosion, which suggests that F1, F2 and F3 were either blind faults, or were synsedimentary faults that were blanketed with sediments during deposition of the Late Jurassic to Early Cretaceous syn-rift sequence (Underhill, 1991b, a; Nicol et al., 1997; Childs et al., 2003). Analysis of throws on the mapped faults shows that F1, F2 and F3 have vertical displacement gradients greater then ca. 0.16 (Fig. 5). This value is consistent with vertical displacement gradients calculated for synsedimentary faults in other areas (Nicol et al., 1996; Nicol et al., 1997; Cartwright et al., 1998; Walsh et al., 2003a). Furthermore, the boundaries

between sub-horizontal and sub-vertical throw contours, which separate pre- and syn-faulting parts of the fault surface (Childs et al., 2003), coincide with the base of the regional syn-rift sequence (TopA horizon; Fig. 5). These observations suggest that faults F1, F2 and F3 were active during the deposition of the Upper Jurassic syn-rift sequences (Figs 3 and 4; H5-H1). This inference is consistent with previous studies that have also shown similar faults in the IMF to be synsedimentary in origin (Underhill, 1991a, b; Nicol et al., 1997; Childs et al., 2003; Walsh et al., 2003a). Together, our observations suggest that sedimentation rates generally outpaced fault displacement rates throughout Late Jurassic to Early Cretaceous extension (Childs et al., 2003). Importantly, the synsedimentary character of these faults enabled them to interact with the free surface, facilitating the development of fault-propagation folds (Sharp et al., 2000; Gawthorpe et al., 2003).

3. Method

3.1. 3D seismic interpretation

The 3D seismic survey used in this study is located over the Beatrice oil field within the central IMF (Fig. 2). The seismic survey has a 12.5 m by 12.5 m inline and crossline spacing. The aerial extent of the study area within the survey is 3 km by 2 km. Velocity information from nearby wells was used to depth convert a seismic section. The velocity data are consistent with a uniform overburden lacking lateral velocity variations (Fig. 6). Therefore, the depth conversion process had a minimal effect on the overall geometries observed, apart from a uniform vertical expansion of the entire section. Relative changes of the fault geometries are negligible between the depth and time sections (Fig. 6). Consequently, to prevent the introduction of additional uncertainties due to depth converting the data, the time-migrated volume was used to analyse fault-related deformation.

Six horizons (H1-H6) that are either cut by or located above the upper tip line of the mapped fault-array were picked on every fifth inline and cross line. Areas of structural complexity were interpreted on every second inline and cross line (25 m spacing).

3.2. Quantifying continuous and discontinuous deformation

3.2.1. Discontinuous deformation (fault throw)

Fault throw is defined as the vertical component of displacement measured between mapped horizon cut-offs (Needham et al., 1996). Throw was measured along sample lines orientated perpendicular to the average strike of the studied

faults. Sample line spacing was 20 m. All faults were assumed to have dip-slip displacements (Underhill, 1991b) and the location of the sample grid was fixed, allowing comparison of displacements on different horizons. A disadvantage of using a fixed, oriented sample gird arises when individual faults are not parallel to the average fault strike for the sample volume. This geometric difference creates a miss-match between fault throw and adjacent continuous displacement, adding noise to the aggregate displacement profiles. In this study, all faults are subparallel so the effect is negligible.

The maximum uncertainty associated with the positions of mapped cut-offs is estimated to be 6 ms TWT. Of this, 4 ms TWT arises from the sampling interval of the seismic data. The remaining uncertainty is associated with errors in correlating the interpreted horizon picks across faults. In areas where the seismic horizons are well imaged, the uncertainty due to errors in correlation approach zero.

The ability to interpret fault offsets in seismic data is controlled by the vertical resolution of the data. At depths similar to those in this study (>1.5–2 seconds TWT or approximately 2 km) only faults with throws greater than 20 m will typically have observable offsets (Townsend et al., 1998). Large sections of the fault surfaces with smaller throws are therefore not resolved through mapping of offset horizons. However, by studying the continuous deformation present beyond the mapped fault tips a greater proportion of the fault-related strain can be measured. This continuous deformation at the scale of observation can be mapped with confidence due to the close spacing of the 3D seismic lines and by minimizing miss-ties on horizon grids.

3.2.2. Continuous deformation (apparent dip)

The vertical component of displacement due to continuous deformation in the volume surrounding the mapped faults was calculated from the apparent dip of triangulated horizon grids. Apparent dip was measured along the same set of sample lines used to calculate fault throw, thus allowing direct comparison with fault throw (Fig. 7). Sensitivity studies were performed on selected horizon grids to determine the optimum triangle size. Large triangles produce smoother surfaces. Smaller triangles more closely match the picked horizon grid, but increase the potential for noise. In this case, “noise” refers to scatter due to natural variability in reflector dip that is not fault-related, miss-correlations of horizon grids across faults and the inherent uncertainty associated with the sample interval of the seismic data. A maximum triangle size of 20 m was used to ensure a representative reconstruction of the raw data.

The next step was to distinguish apparent dips due to continuous deformation in the volume surrounding the mapped fault-array (here termed “abnormal rotations”) from dips caused by regional tilting of each horizon. The half-graben geometry of the IMF means that reflectors display a regional tilt towards the north-west (Fig. 2). Some of the tilt is also likely to result from flexure in the footwall of a major fault located immediately southeast of the studied fault-array (Figs. 2 and 3; (Barnett et al., 1987). The magnitude of regional tilt on each horizon was calculated in areas away from the mapped fault-array, and apparent dips less than or equal to the regional tilt were excluded from further analysis. Large apparent dips can also be caused by miss-ties in horizon grids between adjacent inlines or crosslines (Fig. 8a, point X) and/or by deformation related to other faults (Fig. 8a, point Y). These anomalies were removed by visual inspection and were also excluded from further analysis. The remaining areas of abnormal rotation

were hypothesised to be fault-related continuous deformation in the volume surrounding the studied fault-array (Fig. 8b).

Maps showing the distribution of abnormal rotation around the mapped fault-array were contoured for “low” (≤ 2º), “medium” (2º-4º), “high” (4º-12º) and “very high” (> 12º excluding fault polygons) values of abnormal rotation. As shown previously, depth conversion results in vertical expansion of seismic sections (Fig. 6), allowing comparison of abnormal rotations on different horizons.

Finally, the vertical displacements attributed to continuous fault-related deformation were summed along each sample line, allowing direct comparison with fault-throw measurements (Fig. 9).

4. Results

4.1. Reflector geometries

Horizons H1 to H3 are located above the seismically imaged upper tip line of the fault-array. Horizons H4 to H6 are cut and offset by one or more of the mapped fault segments, F1, F2 and F3 (Fig. 3). Vertical seismic sections oriented approximately perpendicular to fault strike show that the youngest H1 – H3 sequence (and, where it is not faulted, the older H3 – H5 sequence), change in thickness across the underlying fault-array. The points at which younger H1 – H3 sequences achieve their maximum thicknesses are not immediately adjacent to the upward projection of the underlying fault plane, but are located up to 200 m to the northwest, towards the mutual hanging wall of the fault-array (Fig. 3). In contrast, the oldest H5 – H6 sequence is commonly thicker in the immediate hanging walls of the mapped faults (e.g. Fig. 3b, adjacent to fault F1).

Reflector dips vary around the seismically imaged fault tips. Dip values typically increase within regions tens to hundreds of metres wide, situated either side of and/or above mapped upper tip points (Fig. 3 and 9). The steepest horizon dips occur in narrow zones above fault tips (e.g. Fig. 9, left hand side). Steep dips also occur along strike from the lateral tips of seismically imaged faults. These anomalous rotations occur within both pre- and syn-faulting sequences (e.g. Fig. 3b, Horizon H6). In all cases, the anomalous rotations occur in strata that dip towards the mutual hanging wall of the fault-array, giving rise to broad monoclines and sharper kinks (Fig. 3).

4.2. Spatial distribution of continuous deformation

In map view, the patterns of abnormal rotation observed on horizons H1 – H4 are not uniformly distributed above faults F1 and F2, but rather occur as patchy areas of high and low abnormal rotations (Fig. 9, left hand side). Regions of high and very high rotation occur above the seismically imaged tip lines of F1 and F2, expressed as discrete en-echelon bands (dark grey) surrounded by wider zones of more gentle abnormal rotation (light grey) (Fig. 9, horizons H1 – H4). The en-echelon bands of high to very high rotation vary in width between 60 and 300 m and coincide with the projected locations of the seismically imaged faults from below (Fig. 10). The steep limbs of these monoclinal bands are located over the projected hanging wall blocks (Fig. 3).

Horizon H1 is the youngest horizon to have been affected by faults F1 and F2 and marks the uppermost boundary of continuous deformation that can be imaged in the seismic volume. Starting at horizon H1 and working downward toward the mapped upper tip line, the distribution and magnitude of abnormal rotation changes noticeably (Fig. 9). Horizon H1 is characterised by a 750 m wide zone of low abnormal rotations, which trends NNE–SSW and contains patches of medium abnormal rotation (darker grey) that are arranged in a left-stepping en-echelon pattern.

On Horizon H2, an 800 m wide zone of fault-related continuous deformation follows the same NNE – SSW trend as horizon H1. Within this wide zone are three approximately 90 m-wide bands of high to very high abnormal rotations, which trend NE – SW and again have a left-stepping, en-echelon arrangement. The NNE – SSW trend persists for Horizon H3, where the wider zone of

295 continuous deformation contains a continuous band of parallel, NE – SW trending,
296 left-stepping segments that merge to define the overall NNE – SSW trend.
297
298 Horizon H4 is also characterised by a general NNE – SSW trending zone of
299 continuous deformation. Fault F1 intersects H4 (Fig. 9, Horizon H4). The
300 magnitude of continuous deformation is noticeably reduced in the immediate
301 hanging wall of the mapped fault trace (graph, H4, Fig. 9). The greatest
302 magnitude of continuous deformation for this horizon occurs at the fault tips (i.e.
303 directly above the trace of F1 on H5) and above the projected location of F2 (Figs
304 9 and 10).
305
306 Two seismically imaged fault segments cut horizon H5 (Fig. 9). Fault F1 has a
307 maximum throw of approximatley 50 ms at this level. The distribution and amount
308 of continuous deformation on horizon H5 is markedly different as compared to the
309 overlying horizons. The high levels of continuous deformation present on the
310 younger horizons (H2 – H4) are reduced in the immediate foot and hanging walls
311 of F1 and F2 (Fig. 9). However, high levels of continuous deformation extend
312 beyond the mapped south-western tip of fault F1 to a distance approximately
313 equal to the length of the fault trace seen on the underlying horizon H6 (Fig. 9,
314 Horizons H5 – H6, point a). In addition, NE-SW and E-W trending bands showing
315 high levels of continuous deformation occur, respectively, at the tips of F2 and
316 within the relay zone between F1 and F2.
317
318 Horizon H6 is cut by three seismically imaged fault segments, and displays
319 minimal continuous deformation in the hanging wall of fault F1. The southwestern
320 tip of fault F1 also displays smaller magnitudes of continuous deformation
321 compared to the same region on H5. Horizon H6 contains the maximum along-

strike extent of fault F1 hence there are no (seismically imaged) fault tip lines that lie directly beneath the mapped tip of F1 (Fig. 5). The immediate footwall of fault F1 is characterised by a band of continuous deformation adjacent to a prominent right-stepping bend in the fault trace (Fig. 9, Horizon H6, point b). This band of anomalous dips follows the same trend as the fault trace immediately to the north-east of the right-stepping bend.

4.3. Displacement distance profiles

The displacement distance (d-x) profiles (Fig. 9, right hand side) show the vertical offsets (throws) on faults F1, F2 and F3 together with the vertical component of continuous displacement calculated from the areas of abnormal rotations (Fig. 9, left hand side). The d-x plots are therefore a graphical representation of the discontinuous and continuous displacements for each horizon.

The maximum aggregate vertical component of displacement decreases from approximately 140 ms on H6 to about 80 ms on the overlying H5 horizon, but has an approximately constant value of between 40 and 50 ms on horizons H2 to H4. The maximum aggregate component on H1 is about 20 ms. The along-strike extent of the region affected by faulting and/or continuous deformation displays a similar pattern. The southwestern “tip point” of the deformation zone is situated about 300 m further towards the NE on horizon H5 compared with H6, and by about 1200 m in the same direction on H4 compared with H5. By contrast, the tip of the deformation zone maintains an approximately constant position for horizons H1 – H4.

Continuous displacement accounts for a significant proportion of the total deformation observed on each horizon. Horizons H6-H5 have approximately equal amounts of displacement partitioned between continuous deformation and mappable fault offsets (Fig.9). Horizons H1-H3 are entirely deformed by continuous deformation while horizon H4 is nearly all continuous deformation.

On each horizon, the total displacement curve (dashed line) resembles that of a single fault more than either the fault displacement or continuous displacement curves alone (Fig. 9). Close inspection of the d-x plots shows striking inverse correlations between the observed magnitudes of continuous and discontinuous displacement (Fig. 9). For example, abrupt increases in the magnitude of continuous displacement occur at the northeast tip of F2 and southwest tip of F1 on horizon H5, which helps to “smooth out” the total displacement profile (Fig. 9, H5). Similarly, midway along the strike of F2 a low in fault displacement is matched by an increase in continuous displacement (Fig. 9, H5). These relationships maintain an aggregate profile that resembles one for a single fault. Similar relationships can be observed on the other horizons (Fig. 9, H4-H6). The displacement profiles derived solely from continuous displacement on horizons H1 – H3 are also seen to resemble that of a single coherent fault. Thus, displacement profiles resembling that of a single coherent fault are present at all levels within the sequence.

4.4 Description of fault F1

Fault F1 has a maximum throw of 115 ms TWT decreasing towards the mapped southwestern tip. Fault F1 displays its maximum lateral extent on horizon H6 and decreases in length upwards to horizon H4 (Figs 9, 10). Horizon H6 is

characterized by a zone of abnormal rotation that extends 100 m beyond the mapped fault, but the horizontal extent of the region of abnormal deformation increases upwards between horizons H6 – H4 (Fig. 10). The tip line of fault F1 directly underlies Horizons H5 and H4. Therefore, a correlation exists between an increase in the extent of abnormal rotation beyond the mapped fault tip and the presence of a seismically imaged fault plane immediately beneath those horizons. The transition from the sandstone-dominated pre-rift strata to the shale-dominated syn-rift sequence occurs at horizon H5 (Fig. 3). This transition also marks an increase in the ratio of continuous deformation to fault displacement, and the appearance of a wide zone of low to medium rotation, measured normal to strike (Fig. 9). Above fault F1 (H4-H1) is a zone of strong abnormal rotation. This zone splits into three distinct linear bands on horizon H2. These zones of abnormal rotation trend NW-SE matching the mapped fault below.

5. Interpretation and discussion

5.1. Geometric coherence

A consequence of syntectonic sedimentation, such as that inferred in the study area, is the development of different sediment thicknesses in the hanging wall and footwall of mapped faults. Therefore, it is important to consider the role of differential compaction in producing rotated seismic reflectors and apparent monoclinal geometries, as reported by Thomson and Underhill (1993) elsewhere in the IMF basin. Compactional drapes are likely to be greatest within depocentres containing the thickest syn-faulting sequences. This situation will occur towards the centres of faults, that is, closest to the point of maximum throw. However, our observations show that continuous rotations of seismic reflectors are likely to be greatest at fault tips, not within the hanging walls of seismically imaged fault traces. Similarly, rotated reflectors can also be seen within the pre-growth (pre-H5) sequence, which was presumably well-compacted prior to the onset of faulting. Some compactional drapes interpreted by Thomson and Underhill (1993, their fig. 5) are related to faults with marked convex-upward geometries, whereas the faults in the present study area are sub-planar (Fig. 3c). We conclude that the observed abnormal rotations were primarily a response to fault growth and propagation, rather than differential compaction. However, differential compaction may have subsequently exaggerated stratal dips and monoclinal geometries.

Our results show that the continuous deformation in the volume surrounding the upper part of the mapped normal fault-array is characterised by rotations of seismic reflectors, resulting in increased dips towards the mutual hanging wall. These “abnormal rotations” give rise to broad monoclines and sharper kinks. In

map view, regions of continuous deformation appear to be patchily but systematically distributed, with the greatest magnitudes of abnormal rotation occurring above or along strike from mapped upper and lateral fault tip points, adjacent to bends in fault traces, and within relay zones (Fig. 9). The vertical component of displacement calculated from the continuous deformation acts to "fill-in" missing displacement in the throw profile for the aggregate fault-array (Fig. 9). The aggregate displacement profile more closely resembles that of a single fault than either the fault throw or continuous displacement profiles alone (Huggins et al., 1995; Walsh et al., 2003b). The mapped structures therefore appear to have developed as part of a single, coherent fault-array.

5.2. Fault-propagation folding and the influence of mechanical stratigraphy

In detail, the youngest syn-rift horizon (H1) shows the development of broad monoclines (Fig. 9). Older syn-rift horizons display sharp, NE-SW trending "kinks" (areas of high abnormal rotation) that are situated directly above mapped fault tip lines (Figs 9, 10) within broad regions of more gentle rotation. The kinks become more pronounced and better interconnected on older horizons (H2 – H5, Fig. 9). Trading space for time, we interpret these observations to mean that the broad, low-amplitude folds developed at an early stage of fault propagation but were subsequently deformed by sharper kinks situated directly above propagating tip lines.

This interpretation is consistent with the results of analogue and numerical models that simulate faulting and fault-propagation folding in the sedimentary cover above a predefined "basement" fault (Withjack et al., 1990; Finch et al., 2004). Numerical

models show that deformation of a weak cover sequence is initially characterised by the development of a broad monocline above the basement fault. With increasing slip, deformation becomes more localised above the propagating fault, giving rise to tight fault-propagation folds within the broad monocline (Withjack et al., 1990; Finch et al., 2004). As deformation continues, the limbs of the sharp, kink-like fault-propagation fold steepen until they are finally breached by the propagating fault. By contrast, the presence of a strong cover sequence results in a narrower monocline and more rapid propagation of the basement fault into the cover. These models show that the mechanical strength of the cover sequence is an important control on the development of fault-propagation folds.

The inherent limit in seismic resolution means that it is impossible to quantify the proportion of continuous displacement accommodated by plastic deformation vs. sub-seismic scale faulting, without direct sampling by drilling. Nevertheless, it is important to point out that the fault-propagation folds described in this study have vertical extents (amplitudes) of approximately 40 ms (Fig. 9), which is more than an order of magnitude smaller than comparable seismic examples of fault-propagation folds on the Halten Terrace, offshore Norway (vertical extents between 500 – 1000 ms) (Withjack et al., 1990; Corfield and Sharp, 2000). Here, fault propagation folds developed in a shale-dominated syn-rift sequence overlying pre-rift red beds and evaporites (Marsh et al., 2009). The overall scale of fault-propagation folding is controlled by the size of the underlying faults, but it appears that the geometry and evolution of the folds is controlled by the mechanical properties of the overburden sequence (Withjack et al., 1990).

5.3. Growth of the mapped fault-array

The total displacement profiles (fault throw plus continuous deformation; Fig. 9) show that the along-strike extent of the region affected by fault-related deformation on F1, F2 and F3 is less from the H6 (pre-rift) and H4 (syn-rift) stratigraphic level, but is approximately constant within the overlying syn-rift horizons. Similarly, maximum aggregate displacements are less between horizons H6 to H4, but is nearly constant for H4 to H2 before decreasing again for H1. The near-constant width and along-strike extent of the region affected by fault-related deformation suggests that the volume of continuous deformation surrounding the mapped faults is enclosed by a steeply-plunging (sub-vertical) lateral tip line. The observation of near-constant along-strike length throughout the syn-rift sequence is interpreted to imply that the lateral length of the fault-array was established at an early stage in its growth. This inference is consistent with a previous study that suggests that fault lateral lengths may be near-constant from early fault system development (Walsh et al., 2002).

The small changes in aggregate displacement upward through the H4 to H2 syn-rift succession is consistent with a small vertical displacement gradient above horizon H5 (Fig. 9, right hand side). The near-constant aggregate displacement for these horizons, followed by a decrease in displacement for the youngest syn-rift horizon, H1, could be interpreted as evidence for fault reactivation following a period of stasis during the deposition of H4 to H2, e.g. (Cartwright et al., 1998). However, our preferred interpretation, which requires only a single phase of rifting, is that the small vertical displacement gradients resulted from an increase in the sedimentation rate relative to the displacement rate on the evolving fault-array. This increase in the ratio of sedimentation to fault displacement could have occurred due to an absolute increase in the sedimentation rate, or due to a

492 temporary decrease in fault-slip rate in this part of the IMF basin, cf. (Jackson,
493 1999), or a combination of both mechanisms. In any case, blanketing of the fault
494 scarps facilitated the development of fault-propagation folds in the overburden.
495

496 ### *5.4. Geometry and evolution of fault F1*

497 The lateral tip line of fault F1 in the study area plunges steeply towards the SW
498 (Fig. 10). The northeastern upper tip line is sub-horizontal beneath H4, but
499 southwestward, it curves up and penetrates H4. The lateral “tip line” or boundary
500 of the continuously deformed region around F1 has a similar geometry to the
501 lateral fault tip line, plunging steeply southwestward. The 3D reconstruction
502 clearly shows that regions of high continuous strain, i.e. monoclines, on horizons
503 H4 – H6 directly overlie the lateral tip line of F1. Monoclines observed at fault tips,
504 similar to those seen here, are often recorded in outcrop data (Cartwright and
505 Mansfield, 1998; Jackson et al., 2006; Ferrill et al., 2007). Our results therefore
506 confirm White and Crider’s (2006) suggestion, which was based on outcrop data
507 and linear-elastic boundary-element method modelling, that monoclinal folds are
508 likely to develop above the blind, lateral extents of surface-breaking,
509 synsedimentary faults.
510
511 The reflectors above the mapped upper tip line of fault F1 are deformed by three
512 en-echelon, left-stepping monoclines (fault-propagation folds). The internal
513 structure of the monoclines is below the resolution of the seismic data, but the
514 analysis of the aggregate displacement profiles show that the folds developed as
515 a coherent part of the fault-array. The simplest model to explain the en-echelon
516 arrangement of the monoclines is that the upper tip line of fault F1 bifurcated
517 (split) as it propagated upwards from horizon H5, forming three en-echelon, left-

518 stepping lobes. On H4, the central lobe is visible as the mapped trace of F1 (Fig.
519 9). This interpretation is consistent with previous models for the coherent growth
520 of segmented fault-arrays (Childs et al., 1996b; Marchal et al., 2003; Walsh et al.,
521 2003b). Importantly, our findings show that the distribution of continuous
522 deformation can be mapped and visualised using 3D seismic data, providing a
523 method to study the interactions between primary and secondary fault segments
524 even where the aggregate throw is only a few tens of milliseconds (Fig. 10).
525
526 Analysis of seismic data alone cannot, however, explain all of the observed
527 relationships. In particular, it is not clear as to why anomalous dips are commonly
528 observed to be low or absent in the immediate hanging walls of mapped faults
529 (e.g., Fig. 9). It could be because stratal dips are very high within narrow zones
530 immediately adjacent to the fault traces, hence are not imaged in seismic data.
531 This hypothesis would suggest that reflector dips increase with increasing
532 displacement on adjacent faults. This concept is consistent with continuous
533 deformation originating due to, or being modified by, frictional drag. Alternatively,
534 the absence of continuous deformation may suggest that some segments that
535 propagated upwards and broke the surface more rapidly than in adjacent regions,
536 (Ford et al., 2007).
537

538 ### *5.5. Practical applications*

539 Our results show that areas with abnormal rotations can be used to identify
540 regions of fault-related deformation in 3D seismic data. Correct identification of
541 small-scale fault-related deformation has implications for modelling fluid flow
542 (hydrocarbons, ground water, CO_2) in the subsurface. The method proposed here
543 is versatile and can be used in any tectonic setting and complements existing

techniques used to sample fault throw. Previous studies (e.g., (Steen et al., 1998; Townsend et al., 1998) have suggested that dip anomalies can be used to identify areas of small (sub-seismic) scale faulting in 3D seismic volumes. For example, Figure 9 highlights areas of anomalous rotations within the relay ramp between F1 and F2 on horizon H5, and adjacent to the right-stepping bend in the trace of F2 on H6. The map-view geometries suggest that these areas of continuous deformation may be associated with, respectively, an incipient breaching fault cutting obliquely across the relay ramp and a footwall splay fault associated with a breached relay on F2. The coherency of the aggregate displacement profiles is consistent with these inferences. The key point is that the techniques described here allow rigorous geological analysis of these anomalies, enabling us to investigate possible implications if they are treated as faults or fault-related fracture systems.

6. Conclusions

1. We have calculated the apparent dips for six horizons within a 3D seismic volume, measured along sample lines oriented perpendicular to the average strike of a mapped fault-array. This dip attribute is used to derive the spatial distribution of fault-related continuous deformation, from which we calculated the vertical component of displacement due to continuous deformation. This measure of continuous displacement is directly comparable to fault throw.

2. This technique permits the analysis of continuous deformation structures (fault-propagation folds) that are up to an order of magnitude smaller than previously described.

3. Our study supports previous work, which demonstrated that fault-arrays and associated volumes of continuous deformation surrounding them are geometrically coherent and are likely to have been kinematically coherent throughout their evolution (Walsh and Watterson, 1991; Walsh et al., 2003b).

4. The observation that a fault-array remains coherent as it propagates is not unexpected, if we assume a coherent growth model (Marchal et al., 1998; Walsh et al., 2003b). However, without inclusion of the continuous deformation, the d-x profile for this fault-array could have been miss-interpreted as representing three isolated fault segments with coincidental overlaps.

5. The along-strike extent of the volume of continuous deformation above the upper tip line of the mapped fault-array is approximately constant upwards through the growth sequence, implying that the length of the fault-array was established at an early (small displacement) stage in its development.

6. Analysis of the continuous deformation in the volume above one of the mapped fault segments (F1) reveals a pattern of deformation that is consistent with the distribution of secondary faults expected to develop during tip line bifurcation (Childs et al., 1996b; Marchal et al., 2003). The techniques described in this study can therefore be used to infer the 3D distribution of fault-related strain ahead of propagating fault surface if space is traded for time in the analysis.

7. Our results also confirm previous model predictions that monoclinal folds are likely to develop above the blind, lateral extents of surface-breaking faults (White and Crider, 2006).

8. The analysis of continuous deformation can potentially be used to postulate the existence of sub-seismic scale faults and fracture systems, (e.g., at fault bends and within relay ramps) for the purpose of considering their effects on rock properties and fluid behaviour if the structures were present.

Acknowledgements

We are grateful to Brett Freeman for coding the algorithm that enabled us to use TrapTester software to extract apparent dip data from horizon meshes. Badley Geoscience Ltd. provided academic licenses and training for TrapTester. Dave Stevenson and Gary Wilkinson provided invaluable IT support within the Department of Earth Sciences at Durham University. Brett Freeman and Paul Griffiths provided constructive comments on an earlier version of the manuscript. We are grateful for the constructive reviews provided by Joe Cartwright and Juliet Crider. Bill Dunne provided helpful editorial guidance that improved the clarity of the manuscript. JJL is funded by a NERC Open CASE PhD studentship with BG Group (NE/F006586/1); JI is funded by Statoil UK Ltd.

Figure captions

Fig. 1. Schematic representation structural geometries that produce the appearance of continuous deformation at the scale of observation for a seismic reflection profile. (a) Rotation of the seismic horizon. (b-c) Different arrangements of sub-seismic scale faults. (d) Horizon rotation and sub-seismic scale faults. Taken from (Steen et al., 1998).

Fig. 2. (a) Regional 2D seismic section across the Inner Moray Firth (IMF) basin (section location in Figure 2c). (b) Interpretation of (a) showing the main marker horizons. (See Figure 4 for detailed stratigraphy). The IMF is an extensional half graben with the maximum subsidence against the Helmsdale–Wick basin-bounding fault systems to the NW. (c) Schematic structural geometry of the IMF for the regional base syn-rift stratigraphic horizon (see Figure 4). BCU is the Base Cretaceous Unconformity; Intra Ox. is an Intra Oxfordian reflector that marks the base of the syn-rift sequence in the study area.

Fig. 3. (a-b) Adjacent seismic profiles aligned normal to the strike of the mapped fault-array. The six mapped horizons used in this study are H1-H6 and regional marker horizons are also shown for context. (b) Rotated horizons past the SW tip of fault F1, circled. (c) Time-structure map for horizon H6. The three faults in the study area display a left-stepping, en-echelon arrangement and are separated by relay ramps linking the footwall and hanging wall sediments. A later ENE-WSW trending cross fault, formed during minor post Cretaceous extension, cuts fault F1. Contour measurements are in ms two-way travel time.

Fig. 4. Lithological units from the study area (Beatrice Field), adapted from (Stevens, 1991). Horizons used in this study are highlighted (grey). H1-H5 are in the syn-rift sequence, while H6 is in the pre-rift section.

Fig. 5. Plots of fault throw with contour interval of 10 ms TWT. Throw values go up to 120 ms TWT (darkest colour). The hanging wall cutoff for horizon TopA (Top A Sand, Figure 4) is marked on the plots and represents the base of the syn-rift sequence. (a) Composite fault image viewed in strike projection, showing the spatial relationship of faults F1, F2 and F3 (See Figure 3c for context). F1 is cut by a later cross fault and continues off the edge of the seismic data to the NE. (b) Throw plots for faults F2 and F3. F2 and F3 are partially linked along a branch line (BL). Vertical throw gradients are measured for each fault from the point of maximum displacement to the upper tip line. Vertical throw gradients are 0.5, 1.3, 0.34 and 0.18 for faults F1, F1 continued, F2 and F3 respectively.

Fig. 6. Seismic sections through the study area. (a) Time section. (b) Depth-converted section using velocity information form nearby wells (c). (c) A time-structure map for regional horizon TopA, showing the location of the section and nearby wells. The map is coloured for two-way travel time (TWT), and dark colours equal largest TWT.

Fig. 7. Schematic illustration of displacement measurement for examples of abnormal rotation. The limits of abnormal rotation are defined by the departure from the regional horizon dip. The vertical displacement or throw is calculated for a monoclinal fold.

673 Fig. 8. (a) Areas of abnormal rotation where all apparent dips above the defined
674 background regional values are selected, resulting in the selection of miss-picks
675 and artefacts (X), and geometries on adjacent faults (Y). (b) These features are
676 removed to leave the abnormal rotations attributed to the studied fault-array.
677
678 Fig. 9. Left, map-view distributions of abnormal rotation for each horizon. Each
679 map uses a grey-scale for the magnitude of abnormal rotation (see Figure 8 and
680 main text). White areas are not deformed by F1-F3. Right, displacement distance
681 (d-x) profiles for each horizon. The geographic position of the maps is fixed for
682 each horizon. The graphs record the amount of vertical displacement due to
683 abnormal rotation (shaded areas on maps) and the throws of seismically imaged
684 faults. Graphs (H1 – H6) all show displacement gradually decreasing to the SW.
685 Solid black lines are for continuous deformation, light gray lines are for fault
686 throws, thin black lines are for total fault throw and dashed lines are for the total
687 vertical component of the deformation.
688
689 Fig. 10. A composite 3D view showing the distribution of the high and very high
690 levels of abnormal rotation in the volume surrounding the mapped F1 fault
691 segment. The cross-hatched area represents the mapped F1 fault surface. A
692 variable thickness zone of fault-related deformation encircles fault F1, grey area.
693
694
695

References

Barnett, J., Mortimer, J., Rippon, J., Walsh, J., Watterson, J., 1987. Displacement geometry in the volume containing a single normal fault. AAPG Bulletin 71 (8), 925-937.

Cartwright, J., Bouroullec, R., James, D., Johnson, H., 1998. Polycyclic motion history of some Gulf Coast growth faults from high-resolution displacement analysis. Geology 26 (9), 819-822.

Cartwright, J.A., Mansfield, C.S., 1998. Lateral displacement variation and lateral tip geometry of normal faults in the Canyonlands National Park, Utah. Journal of Structural Geology 20 (1), 3-19.

Childs, C., Watterson, J., Walsh, J.J., 1995. Fault overlap zones within developing normal fault systems. Journal of the Geological Society of London 152 (3), 535-549.

Childs, C., Nicol, A., Walsh, J.J., Watterson, J., 1996a. Growth of vertically segmented normal faults. Journal of Structural Geology 18 (12), 1389-1397.

Childs, C., Watterson, J., Walsh, J.J., 1996b. A model for the structure and development of fault zones. Journal of the Geological Society of London 153 (3), 337-340.

Childs, C., Nicol, A., Walsh, J.J., Watterson, J., 2003. The growth and propagation of synsedimentary faults. Journal of Structural Geology 25 (4), 633-648.

Corfield, S., Sharp, I.R., 2000. Structural style and stratigraphic architecture of fault propagation folding in extensional settings: a seismic example from the Smørbukk area, Halten Terrace, Mid-Norway. Basin Research 12 (3-4), 329-341.

722 Crider, J.G., Pollard, D.D., 1998. Fault linkage: Three-dimensional mechanical
723 interaction between echelon normal faults. Journal of Geophysical
724 Research B: Solid Earth 103 (B10), 24,373-24,391.
725 Ferrill, D.A., Morris, A.P., Smart, K.J., 2007. Stratigraphic control on extensional
726 fault propagation folding: Big Brushy Canyon monocline, Sierra Del
727 Carmen, Texas. In: Jolley, S., Barr, D., Walsh, J.J., Knipe, R.J. (Eds.),
728 Structurally complex reservoirs. Geological Society, London, Special
729 Publications 292, pp. 203-217.
730 Finch, E., Hardy, S., Gawthorpe, R., 2004. Discrete-element modelling of
731 extensional fault-propagation folding above rigid basement fault blocks.
732 Basin Research 16 (4), 489-506.
733 Ford, M., Le Carlier De Veslud, C., Bourgeois, O., 2007. Kinematic and geometric
734 analysis of fault-related folds in a rift setting: The Dannemarie basin, Upper
735 Rhine Graben, France. Journal of Structural Geology 29 (11), 1811-1830.
736 Gawthorpe, R.L., Jackson, C.A.L., Young, M.J., Sharp, I.R., Moustafa, A.R.,
737 Leppard, C.W., 2003. Normal fault growth, displacement localisation and
738 the evolution of normal fault populations: the Hammam Faraun fault block,
739 Suez rift, Egypt. Journal of Structural Geology 25 (6), 883-895.
740 Huggins, P., Watterson, J., Walsh, J.J., Childs, C., 1995. Relay zone geometry
741 and displacement transfer between normal faults recorded in coal-mine
742 plans. Journal of Structural Geology 17 (12), 1741-1755.
743 Jackson, C.A.L., Gawthorpe, R.L., Sharp, I.R., 2006. Style and sequence of
744 deformation during extensional fault-propagation folding: examples from
745 the Hammam Faraun and El-Qaa fault blocks, Suez Rift, Egypt. Journal of
746 Structural Geology 28 (3), 519-535.
747 Jackson, J., 1999. Fault death: a perspective from actively deforming regions.
748 Journal of Structural Geology 21 (8-9), 1003-1010.

749 Kristensen, M.B., Childs, C.J., Korstgård, J.A., 2008. The 3D geometry of small-
750 scale relay zones between normal faults in soft sediments. Journal of
751 Structural Geology 30 (2), 257-272.
752 Marchal, D., Guiraud, M., Rives, T., Van Den Driessche, J., 1998. Space and time
753 propagation processes of normal faults. In: Jones, G., Fisher, Q.J., Knipe,
754 R.J. (Eds.), Faulting, fault sealing and fluid flow in hydrocarbon reservoirs.
755 Geological Society, London, Special Publications 147, pp. 51-70.
756 Marchal, D., Guiraud, M., Rives, T., 2003. Geometric and morphologic evolution
757 of normal fault planes and traces from 2D to 4D data. Journal of Structural
758 Geology 25 (1), 135-158.
759 Marsh, N., Imber, J., Holdsworth, R., Brockbank, P., Ringrose, P., 2009. The
760 structural evolution of the Halten Terrace, offshore Mid-Norway:
761 extensional fault growth and strain localisation in a multi-layer brittle–
762 ductile system. Basin Research, DOI: 10.1111/j.1365-2117.2009.00404.x.
763 Mcgrath, A.G., Davison, I., 1995. Damage zone geometry around fault tips.
764 Journal of Structural Geology 17 (7), 1011-1024.
765 Needham, D., Yielding, G., Freeman, D., 1996. Analysis of fault geometry and
766 displacement patterns. In: Buchanan, P.G., Nieuwland, D.A. (Eds.),
767 Modern Developments in Structural Interpretation,Validation and Modelling.
768 Geological Society London Special Publications 99, pp. 189-200.
769 Nicol, A., Watterson, J., Walsh, J.J., Childs, C., 1996. The shapes, major axis
770 orientations and displacement patterns of fault surfaces. Journal of
771 Structural Geology 18 (2-3), 235-248.
772 Nicol, A., Walsh, J.J., Watterson, J., Underhill, J.R., 1997. Displacement rates of
773 normal faults. Nature 390 (6656), 157-159.

774 Peacock, D.C.P., Sanderson, D.J., 1991. Displacements, segment linkage and
775 relay ramps in normal fault zones. Journal of Structural Geology 13 (6),
776 721-733.
777 Peacock, D.C.P., 2002. Propagation, interaction and linkage in normal fault
778 systems. Earth-Science Reviews 58 (1-2), 121-142.
779 Sharp, I., Gawthorpe, R., Underhill, J., Gupta, S., 2000. Fault-propagation folding
780 in extensional settings: Examples of structural style and synrift sedimentary
781 response from the Suez rift, Sinai, Egypt. Bulletin of the Geological Society
782 of America 112 (12), 1877-1899.
783 Steen, O., Sverdrup, E., Hanssen, T.H., 1998. Predicting the distribution of small
784 faults in a hydrocarbon reservoir by combining outcrop, seismic and well
785 data. In: Jones, G., Fisher, Q.J., Knipe, R.J. (Eds.), Faulting, fault sealing
786 and fluid flow in hydrocarbon reservoirs. Geological Society Special
787 Publication 147, pp. 27-50.
788 Stevens, V., 1991. The Beatrice Field, Block 11/30a, UK North Sea. Geological
789 Society, London, Memoirs 14 (1), 245-252.
790 Thomson, K., Underhill, J.R., 1993. Controls on the development and evolution of
791 structural styles in the Inner Moray Firth Basin. In: Parker, J.R. (Ed.),
792 Petroleum Geology of Northwest Europe: Proceedings of the 4th
793 Conference, The Geological Society, London, pp. 1167-1178.
794 Townsend, C., Firth, I., Westerman, R., Kirkevollen, L., Harde, M., Andersen, T.,
795 1998. Small seismic-scale fault identification and mapping. In: Jones, G.,
796 Fisher, Q.J., Knipe, R.J. (Eds.), Faulting, fault sealing and fluid flow in
797 hydrocarbon reservoirs. Geological Society, London, Special Publications
798 147, pp. 1-25.

799 Trudgill, B., Cartwright, J., 1994. Relay-ramp forms and normal-fault linkages,
800 Canyonlands National Park, Utah. Geological Society of America Bulletin
801 106 (9), 1143.
802 Underhill, J.R., 1991a. Controls on Late Jurassic seismic sequences, Inner Moray
803 Firth, UK North Sea; a critical test of a key segment of Exxon's original
804 global cycle chart. Basin Research 3 (2), 79-98.
805 Underhill, J.R., 1991b. Implications of Mesozoic-Recent basin development in the
806 western Inner Moray Firth, UK. Marine and Petroleum Geology 8 (3), 359-
807 369.
808 Walsh, J., Childs, C., Imber, J., Manzocchi, T., Watterson, J., Nell, P., 2003a.
809 Strain localisation and population changes during fault system growth
810 within the Inner Moray Firth, Northern North Sea. Journal of Structural
811 Geology 25 (2), 307-315.
812 Walsh, J.J., Watterson, J., 1991. Geometric and kinematic coherence and scale
813 effects in normal fault systems. In: Roberts, A.M., Yielding, G., Freeman, B.
814 (Eds.), The geometry of normal faults. Geological Society, London, Special
815 Publications 56, pp. 193-203.
816 Walsh, J.J., Nicol, A., Childs, C., 2002. An alternative model for the growth of
817 faults. Journal of Structural Geology 24 (11), 1669-1675.
818 Walsh, J.J., Bailey, W.R., Childs, C., Nicol, A., Bonson, C.G., 2003b. Formation of
819 segmented normal faults; a 3-D perspective. Journal of Structural Geology
820 25 (8), 1251-1262.
821 White, I.R., Crider, J.G., 2006. Extensional fault-propagation folds: mechanical
822 models and observations from the Modoc Plateau, northeastern California.
823 Journal of Structural Geology 28 (7), 1352-1370.

824 Willemse, E.J.M., 1997. Segmented normal faults: correspondence between
825 three-dimensional mechanical models and field data. Journal of
826 Geophysical Research 102 B1 675-692.
827 Withjack, M., Olson, J., Peterson, E., 1990. Experimental models of extensional
828 forced folds. AAPG Bulletin 74 (7), 1038-1054.
829 Withjack, M., Callaway, S., 2000. Active normal faulting beneath a salt layer: an
830 experimental study of deformation patterns in the cover sequence. AAPG
831 Bulletin 84 (5), 627-651.
832
833

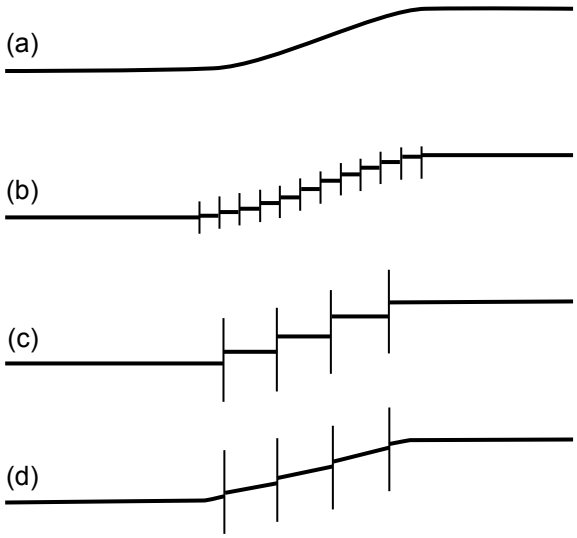

Figure: 1

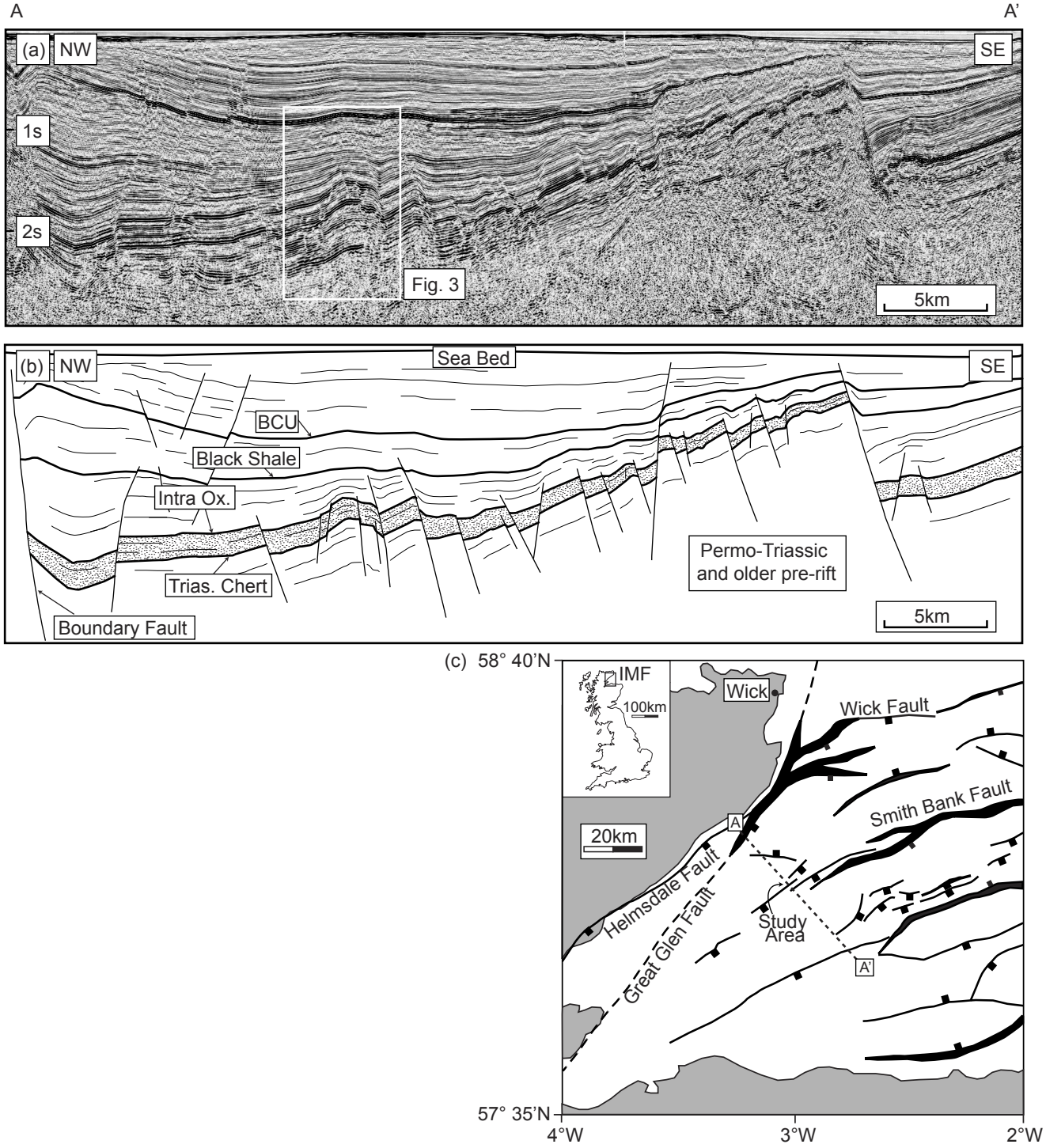
A
A'
(a) NW
SE
1s
2s
Fig. 3
5km
(b) NW
Sea Bed
SE
BCU
Black Shale
Intra Ox.
Trias. Chert
Boundary Fault
Permo-Triassic
and older pre-rift
5km
(c) 58° 40'N
IMF
100km
Wick
Wick Fault
Smith Bank Fault
A
20km
Helmsdale Fault
Great Glen Fault
Study
Area
A'
57° 35'N
4°W
3°W
2°W

Figure: 2

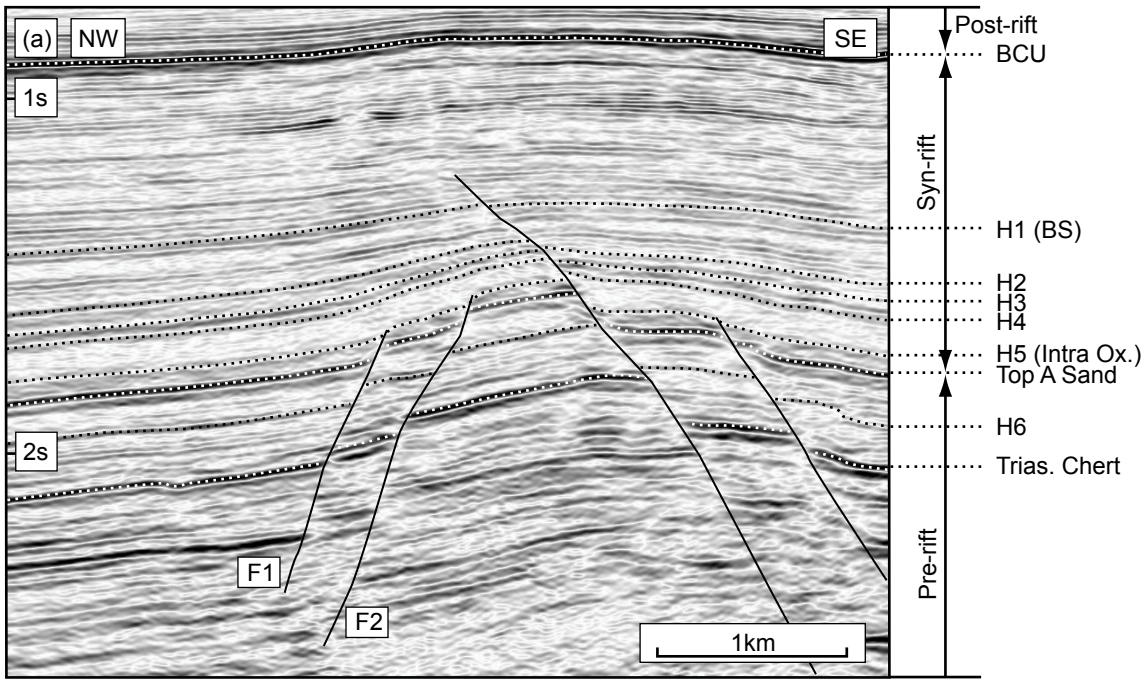

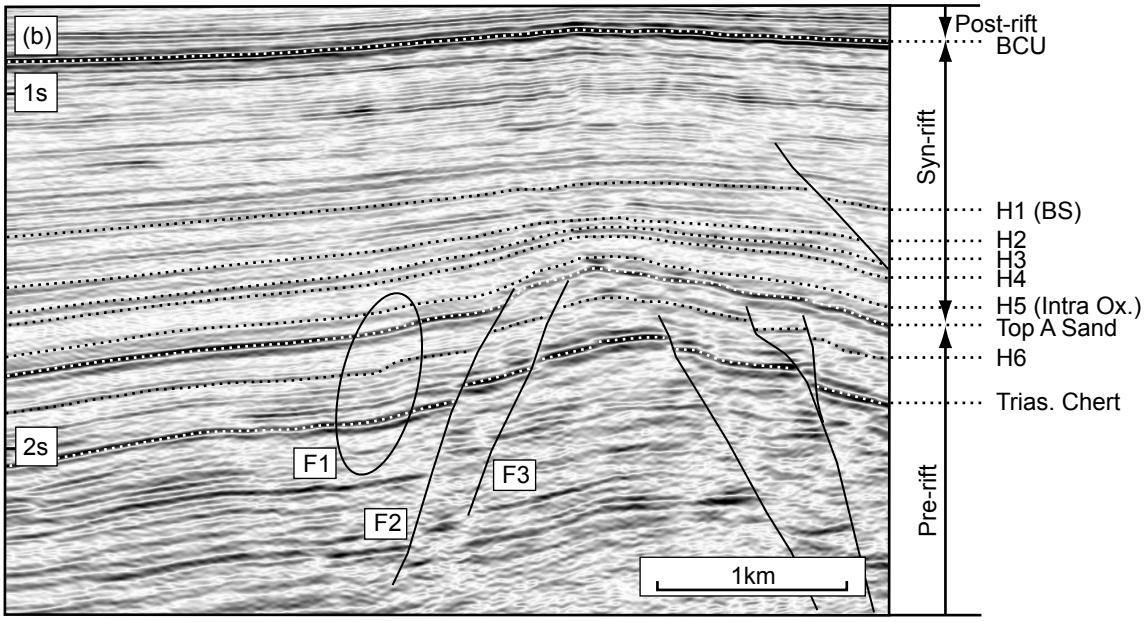

(c)

Fig. 5: View point

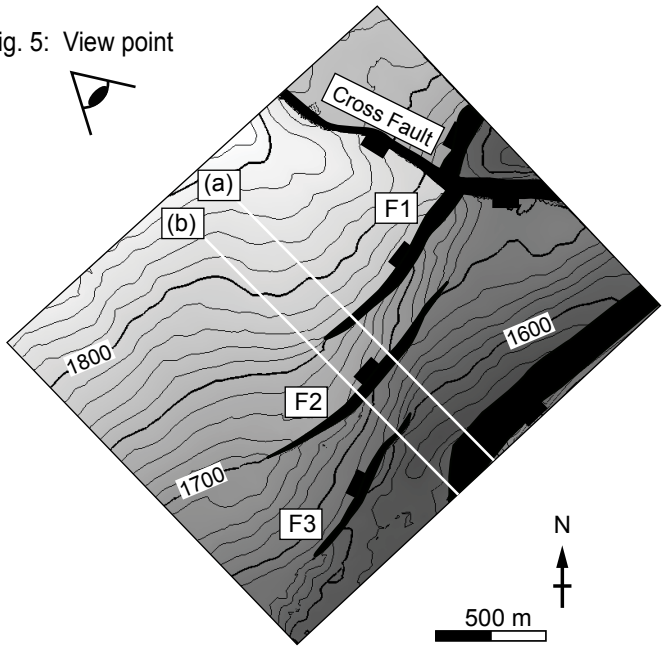

Figure: 3

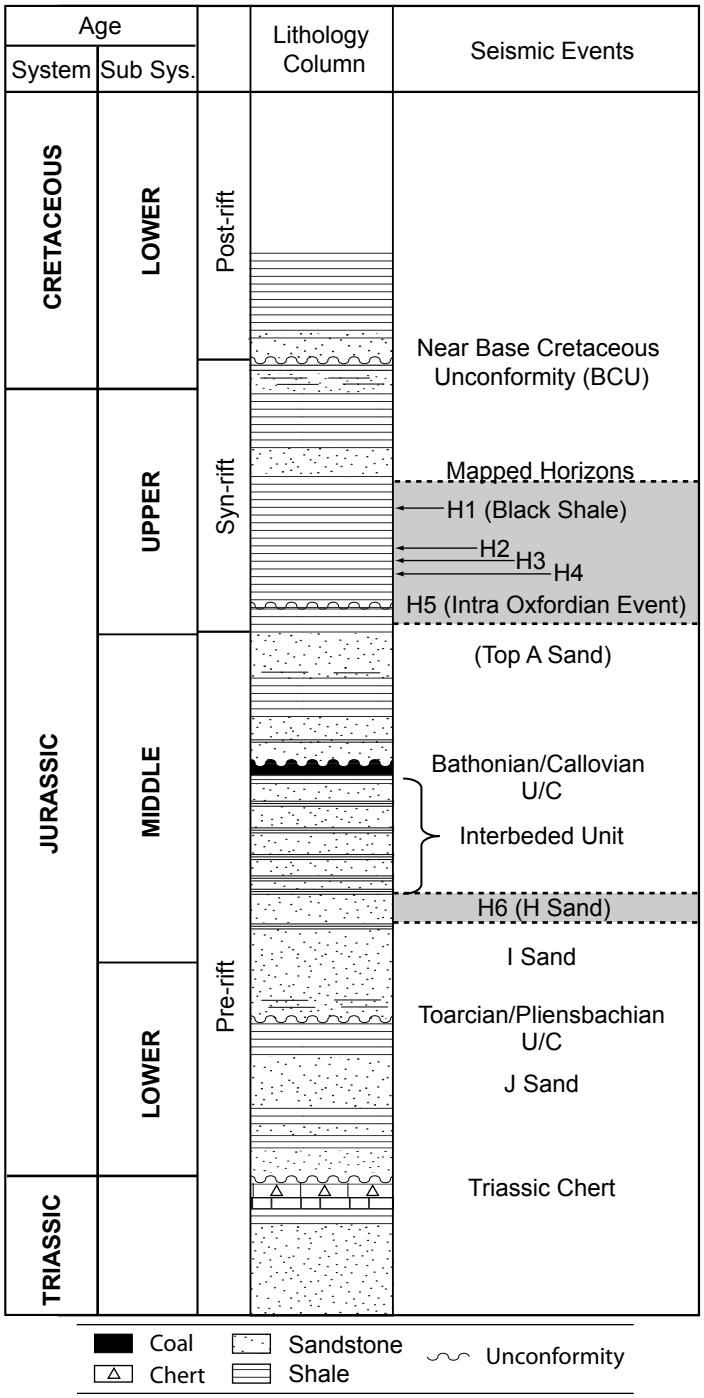
Age
System
Sub Sys.
Lithology Column
Seismic Events
CRETACEOUS
LOWER
JURASSIC
UPPER
MIDDLE
LOWER
TRIASSIC
Post-rift
Syn-rift
Pre-rift
Near Base Cretaceous Unconformity (BCU)
Mapped Horizons
H1 (Black Shale)
H2
H3
H4
H5 (Intra Oxfordian Event)
(Top A Sand)
Bathonian/Callovian U/C
Interbeded Unit
H6 (H Sand)
I Sand
Toarcian/Pliensbachian U/C
J Sand
Triassic Chert
Coal
Chert
Sandstone
Shale
Unconformity

Figure: 4

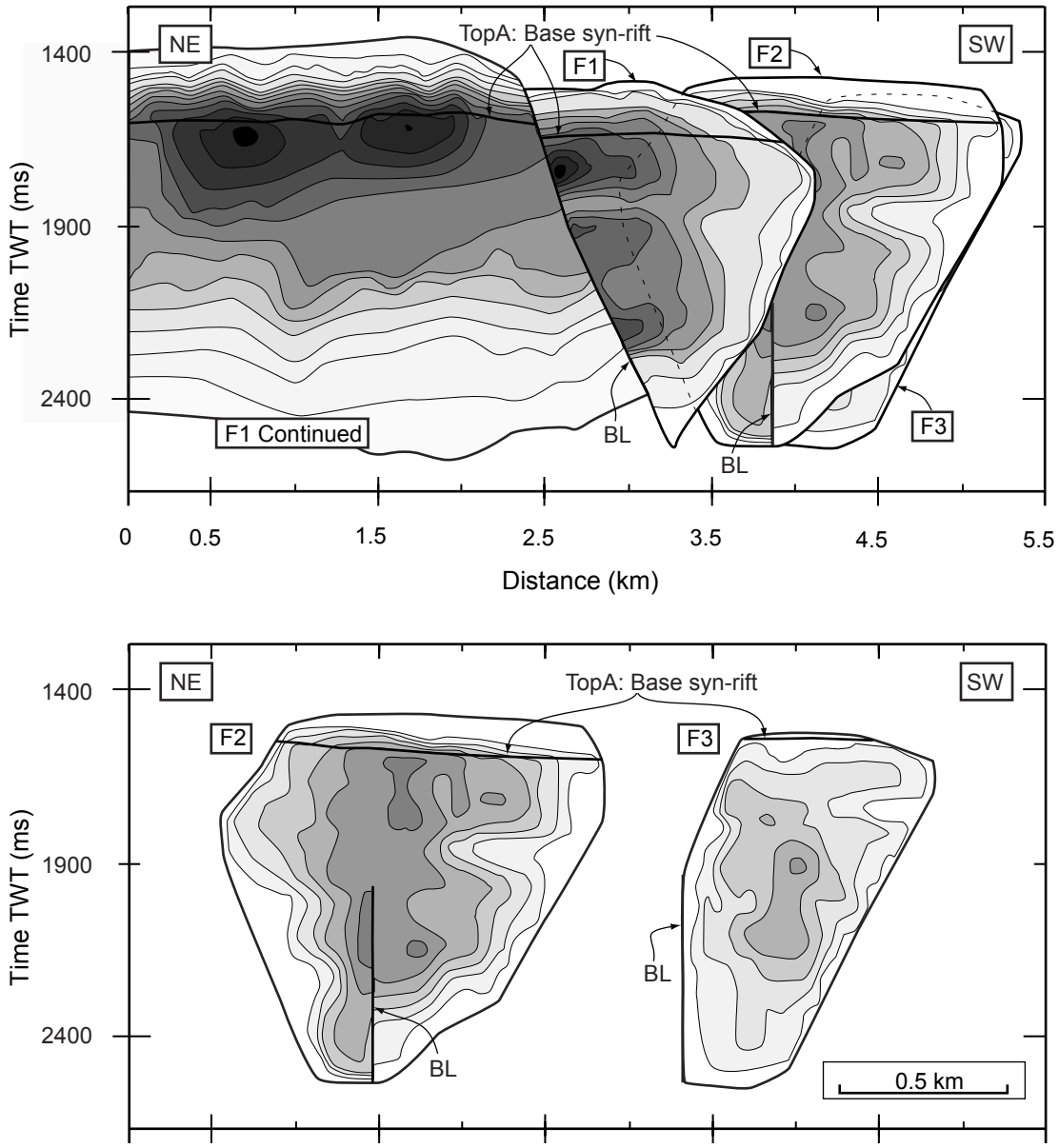
NE
SW
TopA: Base syn-rift
F1
F2
F3
F1 Continued
BL
BL
BL
1400
1900
2400
Time TWT (ms)
0
0.5
1.5
2.5
3.5
4.5
5.5
Distance (km)
NE
SW
TopA: Base syn-rift
F2
F3
BL
BL
0.5 km
1400
1900
2400
Time TWT (ms)

Figure: 5

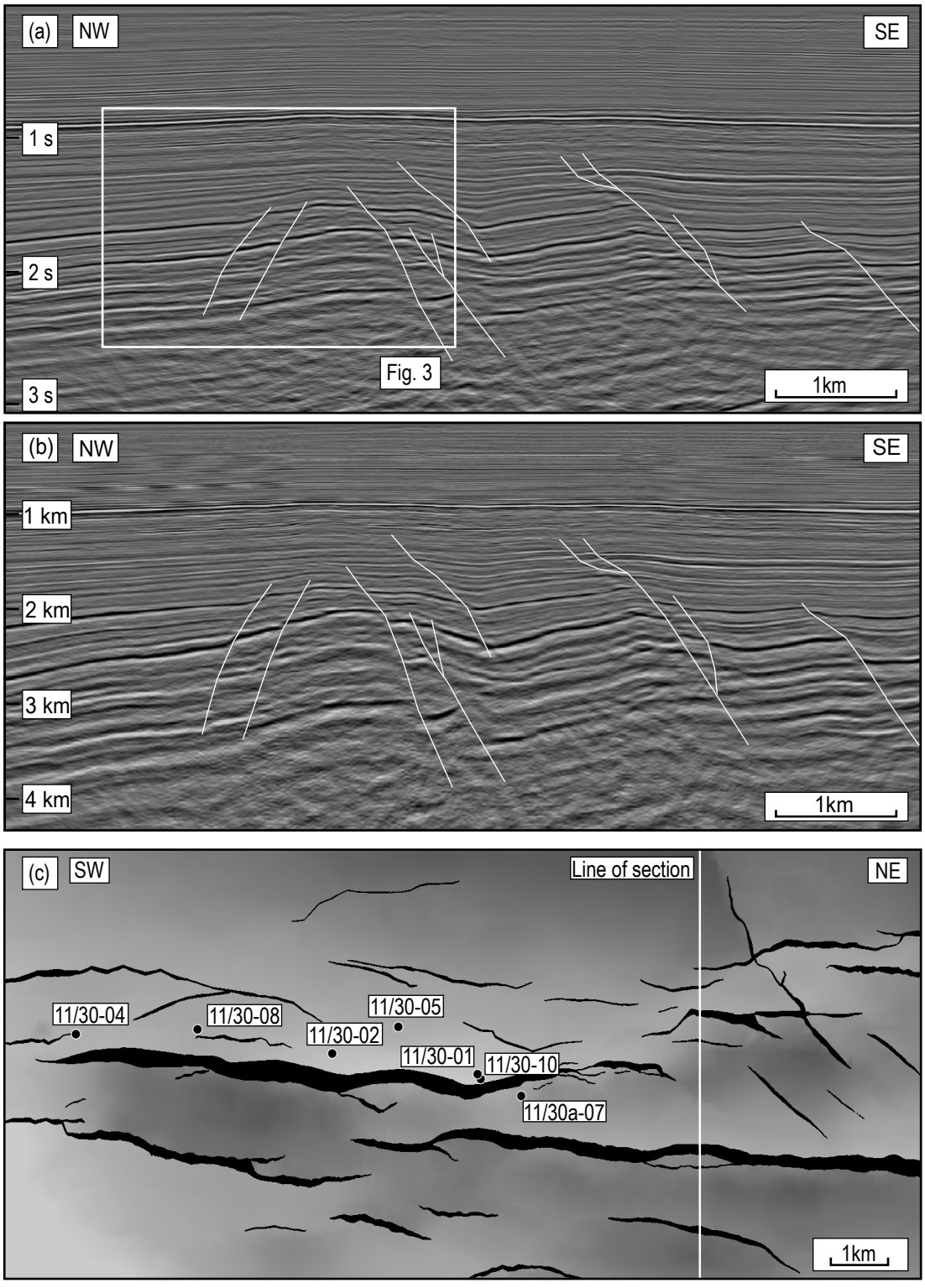
(a)
NW
SE
1 s
2 s
3 s
Fig. 3
1km
(b)
NW
SE
1 km
2 km
3 km
4 km
1km
(c)
SW
Line of section
NE
11/30-04
11/30-08
11/30-02
11/30-05
11/30-01
11/30-10
11/30a-07
1km

Figure: 6

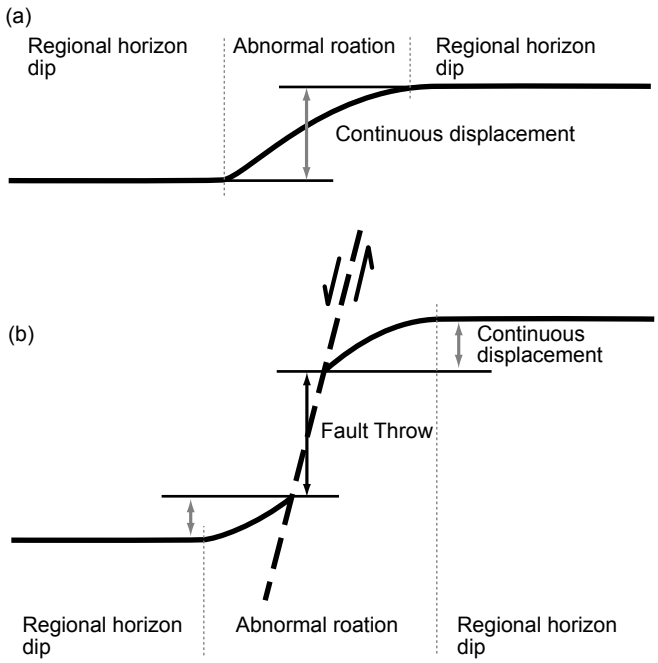
(a)
Regional horizon dip
Abnormal roation
Regional horizon dip
Continuous displacement
(b)
Continuous displacement
Fault Throw
Regional horizon dip
Abnormal roation
Regional horizon dip

Figure: 7

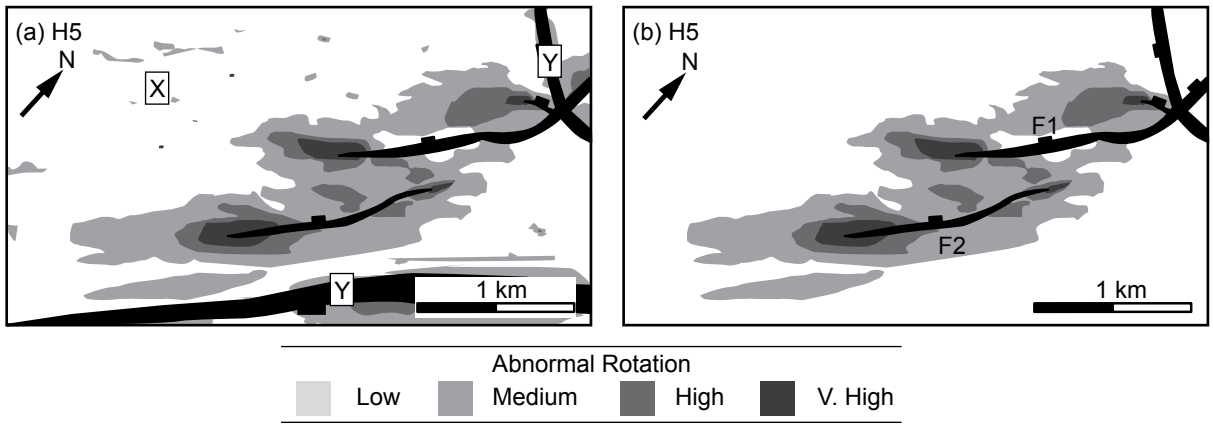
(a) H5
N
X
Y
Y
1 km
(b) H5
N
F1
F2
1 km
Abnormal Rotation
Low
Medium
High
V. High

Figure: 8

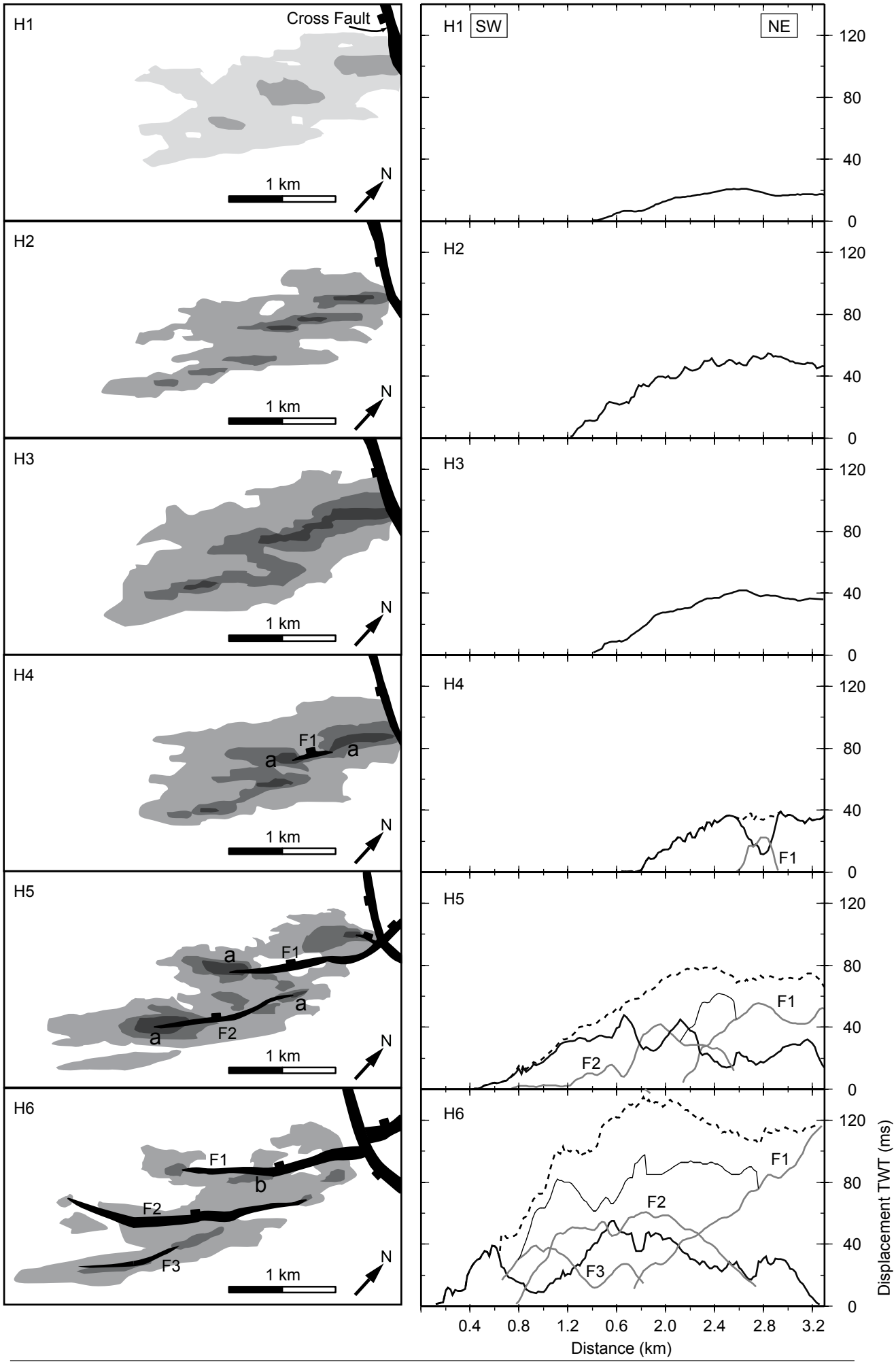
H1
Cross Fault
1 km
N
H1 SW
NE
120
80
40
0
H2
H3
H4
F1
a
H5
F2
H6
b
F3
0.4
0.8
1.2
0.6
2.0
2.4
2.8
3.2
Distance (km)
Displacement TWT (ms)
Abnormal Rotation
Low
Medium
High
V. High
Fault throw
Total fault throw
Total displacement
Continuous displacement

Figure: 9

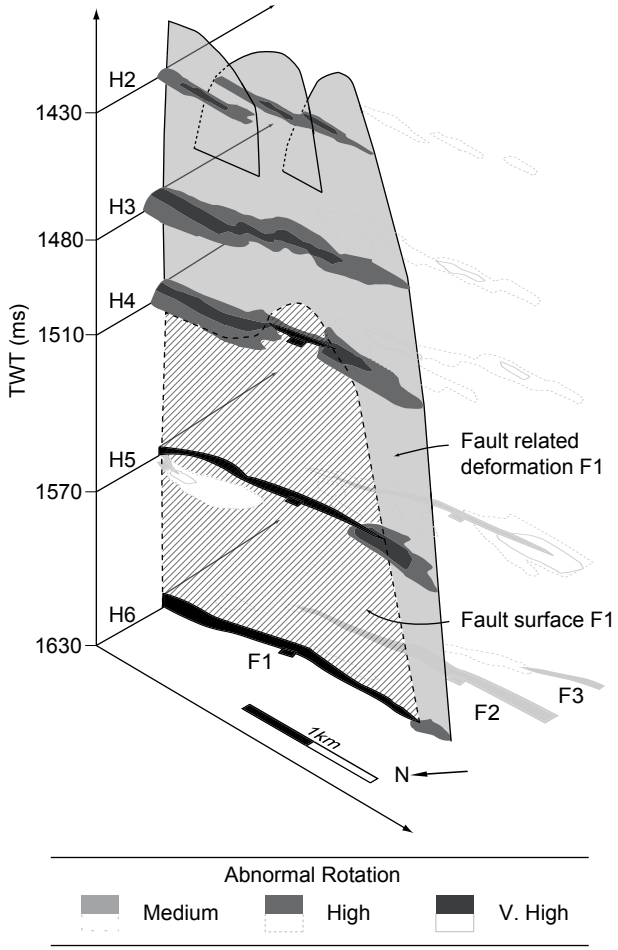
H2
1430
H3
1480
H4
1510
TWT (ms)
H5
1570
H6
1630
Fault related
deformation F1
Fault surface F1
F1
F2
F3
1km
N
Abnormal Rotation
Medium
High
V. High

Figure: 10